In-situ Layer-wise Certification for Direct Laser Deposition Processes based on Thermal Image Series Analysis

Mehrnaz Noroozi Esfahani<sup>1</sup>, Mahathir Bappy<sup>1</sup>, Linkan Bian<sup>1,2</sup>, and Wenmeng Tian<sup>1,2</sup>\*

<sup>1</sup> Department of Industrial and Systems Engineering, Mississippi State University, Mississippi State, MS 39762

<sup>2</sup> Center for Advanced Vehicular Systems (CAVS), Mississippi State University, MS 39762

Abstract: In direct laser deposition (DLD) processes, process uncertainty leads to defects in the final product, which can significantly compromise product quality, mechanical properties, and reliability of the additively manufactured (AM) parts. Therefore, quality control and certification are of critical importance in the broader adoption of DLD processes. *In-situ* thermal history contains critical information of process quality and defect occurrences. This paper proposes a new layer-wise anomaly detection method for *in-situ* DLD process certification by leveraging thermal image series analysis. Image registration is leveraged to characterize the dynamics in the layer-wise thermal history, and Gaussian process (GP) models are used to characterize the variation component which is left unexplained by the image registration operation. Multiple new layer-wise features are extracted from the registration modeling and the GP models. Both a thin wall specimen and a cylindrical shaped specimen are used in the case study to demonstrate the effectiveness of the proposed method. When comparing with the benchmark method, the proposed method shows comparable results for the thin wall specimen, and it significantly outperforms the benchmark method for the cylindrical shaped specimen. In addition, the average computational time of the proposed method is significantly shorter than the average layer-wise build time, enabling the proposed method to facilitate *in-situ* anomaly detection and process control.

**Keywords**: Additive manufacturing, anomaly detection, direct laser deposition, image processing, *in-situ* monitoring, machine learning, process certification.

### 1. Introduction

The direct laser deposition (DLD) process is one of the laser-based additive manufacturing (AM) processes that can fabricate functional components with complicated geometries and functionally graded material [1]. During the DLD process, feedstock material is continuously delivered in the form of powder or wire, while being melted by a focused laser, gradually forming the final component in a layer-by-layer fashion. The high energy produced by the laser melts the feedstock in the melt pool, and the molten material is solidified on the substrate or the previous layer of the build, forming the newly deposited layer [2, 3]. The flexibility of DLD processes enables their applications in both metallic component fabrication and component repair. However, process uncertainty leads to defects in the AM parts, which will significantly compromise the mechanical properties and reliability of the final parts. This remains the major barriers that prevent broader adoption of AM technology to mission critical applications [4, 5].

Since the DLD process is governed by the complex thermo-mechanical process, the thermal history of the DLD process contains significant process information which can be used for defect detection and part certification. The advancement in sensing technologies has enabled real-time monitoring of thermal history for anomaly detection via infrared thermography, generating thermal image streams with extremely large volume and complex spatiotemporal structure. The existing data-driven approaches utilize statistical methods to identify anomalies from thermal images [6–8]. In most of the studies, the local features are used to predict anomaly which cannot be directly utilized to monitor the profile of an entire deposited layer. This being the case, layer-wise process signatures have been extracted based on two major sensing technologies:

1) optical imaging technology [9]; and 2) thermal imaging technology [10]. Although optical imaging systems are more cost-effective, infrared cameras, such as coaxial pyrometers, provide unique capacities on measuring the temperature distribution over time and space [11]. Figure 1 shows a schematic plot of a DLD fabrication process monitored by a coaxial pyrometer. When a process anomaly occurs, the thermal

image series shows unstable behaviors. For example, when there is an abnormal layer height defect, a significant location shift of the melt pool can be observed in the thermal images. Current layer-wise process feature extraction methods are purely data-driven [10], and are therefore cumbersome to incorporate AM part design information, such as printing trajectory. This may lead to limited performance when applying those methods to the AM fabrication of complex geometries. Therefore, there is a need for layer-wise feature extraction methods that can incorporate the design and printing path information of the AM specimen.

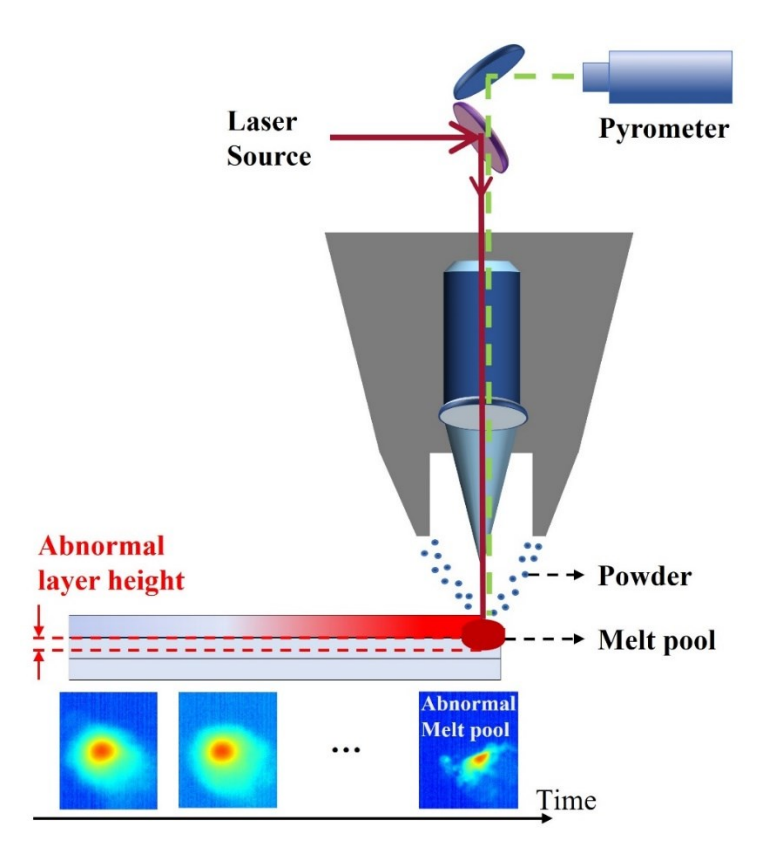


Figure 1: A DLD process monitored by a co-axial pyrometer.

In this paper, the thermal history is formulated as an image-based time series for *in-situ* process certification. A new methodology is proposed to leverage the AM process knowledge to extract layer-wise process features from the real-time thermal history for DLD processes. The major assumption of the proposed methodology is that a stable thermal history leads to homogenous microstructure and porosity-free deposited layers. To quantify the dynamic change in the thermal image series, process features can be

extracted from two sources of variation in the thermal image series, namely, the thermal image registration operation between two consecutive images, and first order difference (i.e., error) between the two thermal images after registration. Subsequently, the extracted layer-wise features are used for process anomaly detection by leveraging supervised learning algorithms, i.e., support vector machine methods.

The technical contributions of the paper are summarized as below.

- The paper proposes a new data-driven formulation to model the layer-wise thermal history by integrating the AM process domain knowledge. More specifically, the melt pool image is decomposed into two components: 1) one is described by the previously observed melt pool image and an image registration operation; and 2) the other is denoted as the error term and modeled as a Gaussian process model.
- The instantaneous printing directions are incorporated into the new formulation to account for complex printing paths. This significantly expands the capacity of the current literature to facilitate anomaly detection for complex shaped specimen fabricated by DLD processes.
- Multiple new layer-wise features, including registration related features and error modeling related features, have been proposed based on the proposed new formulation for process anomaly detection.
- By leveraging a support vector machine classification algorithm, the extracted features can facilitate reliable and efficient *in-situ* layer-wise certification for DLD processes.

The rest of the paper is structured as follows. Section 2 provides a detailed literature review on the existing post-process defect detection techniques, and state-of-the-art studies on *in-situ* process monitoring and anomaly detection for laser-based AM processes. In section 3, the proposed methodology for layer-wise process feature extraction and anomaly detection is introduced. Section 4 presents two case studies of fabricating a thin wall and a cylindrical specimen using the DLD process to validate the proposed methodology. Finally, section 5 summarizes the conclusion and potential future research directions.

#### 2. Literature Review

The state-of-art studies on defect characterization and anomaly detection for laser-based AM can be briefly categorized into two groups, namely, post-manufacturing defect detection and certification (subsection 2.1), and *in-situ* process monitoring (subsection 2.2). Their corresponding research gaps are analyzed at the end of each section, respectively. Subsequently, subsection 2.3 compares the strengths and weaknesses of these two categories of methods.

# 2.1 Post-manufacturing Defect Detection and Part Certification

Most traditional AM defect characterization and part certification methods focus on post-manufacturing inspection, including Computed Topography (CT), Magnetic Resonance Imaging (MRI), and ultrasonic testing [12]–[14]. For example, using the CT adjustment technique by investigating the minimum detectable pore size, the superiority of AM technology over casting processes is investigated [15]. Moreover, X-ray tomography combined with 3D image analysis is applied for the porosity detection in powder feedstock characterization for AM processes [16]. On the other hand, by combining OTSU thresholding and a convolutional neural network (CNN), the porosity is automatically segmented from X-ray CT images of metallic AM specimens [17]. In addition, three techniques (i.e., water intrusion porosimetry, micro-CT, and water absorption under vacuum) have been applied and compared for porosity characterization in [18]. In other studies, it is also shown that the porosity characterization results can vary depending on the collected data (e.g., pore size and pore structure) [19]. However, all of the post-manufacturing quality control approaches for AM can only be used after the final product is completely fabricated. Moreover, those approaches are usually expensive and limited to certain part geometries and/or dimensions.

### 2.2 In-situ Process Monitoring and Anomaly Detection

The metrological systems for *in-situ* anomaly detection in laser-based AM systems can be categorized into two groups, namely, optical imaging and thermal imaging systems. The state-of-the-art process monitoring methodologies developed for both metrological systems are summarized as follows.

The broad adoption of machine vision systems in AM processes leads to various image-based process monitoring approaches for AM. In order to detect and predict the anomalies during production, large amounts of data are generated in the formats of videos or image series which are then analyzed using big data analytics methods. For instance, a novel approach based on spatially weighted principal component analysis (PCA) was proposed to extract the spatiotemporal features from the video data, and the k-means clustering-based method is adopted for automatic defect detection [20]. Moreover, video analysis method was proposed by decomposing the original data into random natural events, sparse spatially clusters, and temporally consistent anomalous events [9]. In addition, a novel CNN architecture was presented for pixel-wise localization of layer-wise powder bed imaging data, and the core advantage of that algorithm is to provide real-time performance, by seamlessly transferring the learned knowledge between different AM machines [2]. Specifically, a computer vision algorithm was recommended to automatically identify anomalies that occur during the powder spreading stage of the process, and the powder bed images are used as the potential component of a real-time control system in an LPBF machine. The developed algorithm was implemented using an unsupervised machine learning approach to detect and classify anomaly [21]. However, all the methods described above are pure data-driven approaches that do not consider the AM process knowledge during the analysis.

Thermal imaging systems provide the temperature measurements in the field of view, and thus they could provide informative characterization of the thermal history for process monitoring and anomaly detection. For example, a reflectometer-based instrument was used to provide the dynamic laser absorption measurements to describe the melt pool dynamics for process monitoring [22]. Moreover, the thermal imaging has been used as an efficient tool in both online monitoring and part certification. For example, Mitchell et al. proposed a methodology for *in-situ* anomaly detection using pyrometry for laser powder bed fusion processes by correlating *in-situ* thermal observations with the included void observed through post-build micro-computed tomography using machine learning algorithms [23]. In another approach, a close-loop control system was developed based on the melt pool characterization using infrared imaging in laser-based AM processes to improve geometric accuracy [24]. Moreover, the melt pools were characterized by image processing and feature extraction from the thermal images, and the supervised machine learning methods were adopted for porosity prediction in a single-track thin wall specimen fabricated by the DLD

process [6]. In addition, Guo et al. developed a data-driven framework that characterizes the spatial-temporal effects for anomaly detection [25]. Moreover, a physics-driven deep learning model was developed to predict the porosity occurrences in the AM parts by integrating both observed and simulated melt pool data [26].

One major limitation in the current studies lies in their underlying premises that the healthy melt pools follow the same distribution. However, the heat transfer varies significantly as the layer is deposited higher in the build, leading to a drifting pattern in the thermal distribution between lower and higher layers. This may potentially limit the performance of the current methods. Seifi et al. [10] proposed a data-driven method to address the thermal distribution drifting by extracting new layer-wise features via tensor decomposition and convex hull computation. However, their method may demonstrate limitations when applied to complex geometry fabrication. As illustrated in Figure 2, during the fabrication of a thin wall specimen, the melt pool images are much more uniform comparing to the ones observed in a cylindrical shaped part fabrication. The variability in the melt pool images of the cylindrical part (in the bottom row) is assignable to the dynamic printing direction, in which the printing starts with the circular perimeter of the layer and then unidirectional infills are printed to form the solid part. Therefore, there is a need in extracting layer-wise features which is capable of accounting for both printing trajectory complexity and thermal distribution drifting.

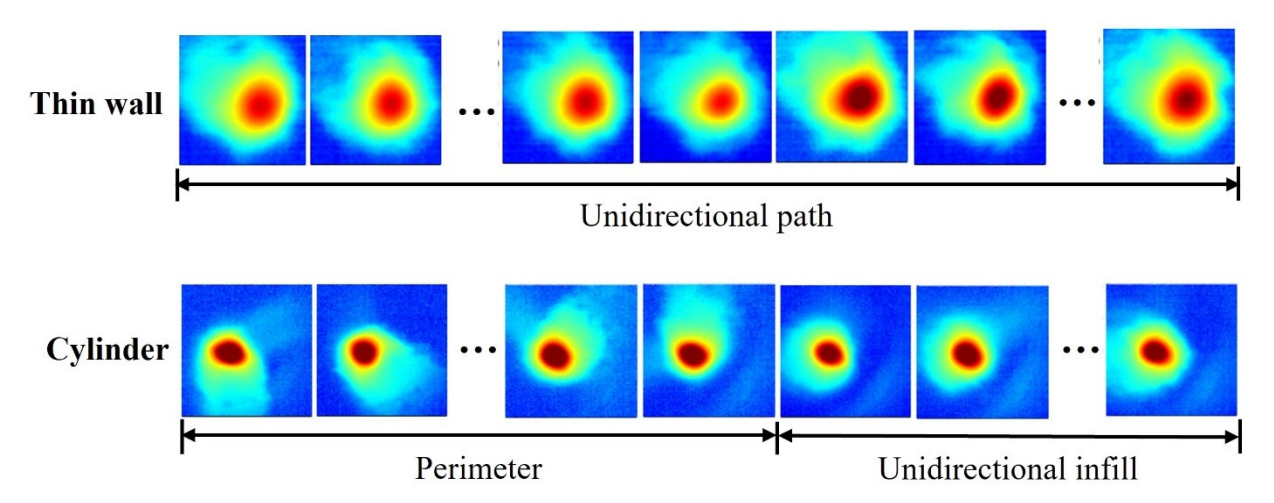


Figure 2: Thermal image examples during the fabrication of one thin wall and one cylindrical shaped specimen.

### 2.3 Comparison of Post-manufacturing and *In-situ* Anomaly Detection

The two major categories of defect characterization and anomaly detection for laser-based AM are compared based on the multiple aspects as below. In terms of measurement accuracy, post-manufacturing methods are, in general, more accurate than the *in-situ* anomaly detection methods. Although post-manufacturing methods demonstrate a wide range of accuracy depending on the technology used, they are all regarded as *direct* characterizations of anomaly and porosity occurrences in the build [27]. However, *in-situ* anomaly detection methods usually leverage *indirect* process characterizations such as thermal history or other process condition variables, which only record the instantaneous process condition during the build to predict the anomaly occurrence in the final AM components [7], [20], [28].

When jointly considering spatial resolution and object size, most post-manufacturing methods, especially the ones using the CT technologies, show a strong linear correlation between the voxel size and the object dimension [12]. Therefore, to measure a large build, post-manufacturing methods need to sacrifice the measurement resolution. However, the resolution of *in-situ* defect characterization methods is determined by the sampling rate of the sensor used [29], and completely independent of the build dimension. Therefore, *in-situ* defect characterization schemes can be more flexibly adapted to large-scale AM certification. In addition, when comparing their measuring speed and equipment cost, post-manufacturing schemes are significantly slower and more expensive than their *in-situ* counterparts [12], [30]. Last but not the least, post-manufacturing schemes cannot facilitate process control during the fabrication while *in-situ* characterization methods can enable real-time feedback control for quality assurance of the AM component [10], [25].

Given their respective strengths and weaknesses, post-manufacturing methods are usually used to collect limited ground truth data in a lab environment to support the training of supervised machine learning models for *in-situ* defect detection [7], [10], [31]. In this sense, the strengths of both categories of methods can be combined to facilitate fast, cost-effective, and accurate AM part certification.

### 3. Methodology

In this section, the proposed methodology is introduced. Subsection 3.1 establishes the overall proposed formulation of the layer-wise thermal history of the DLD process. Subsections 3.2 and 3.3 introduce the two major components in the overall formulation, i.e., image registration and error modeling, respectively. Subsequently, subsection 3.4 introduces the layer-wise features extracted and subsection 3.5 proposes the anomaly detection method based on the features extracted.

### 3.1 Image Series Analysis Formulation

In the DLD process, the melt pool images contain location-based temperature measurements, and the thermal history of a fabricated layer can be considered as a series of melt pool images. To characterize the dynamics in the thermal history, the melt pool image series collected during the build of a layer can be modeled as an image series model as depicted in Equation (1),

$$X_{t+1} = f_{t,t+1}(X_t, \mathbf{\Omega}_{t,t+1}) + \varepsilon_{t+1} \tag{1}$$

where the thermal image collected at time t ( $t \in \mathcal{T}_l$ ) is denoted by  $X_t$  with a dimension of  $I \times J$ , where  $\mathcal{T}_l$  denotes the set of timestamps of collected melt pool images that belong to the l-th layer, and I and J denote the number of rows and columns of each thermal image, respectively.  $f_{t,t+1}$  denotes an image registration function that best aligns  $X_t$  and  $X_{t+1}$ , which is characterized by a 3×3 transformation matrix  $\Omega_{t,t+1}$ . An error matrix denoted by  $\varepsilon_{t+1}$  with a dimension of  $I \times J$  contains the error information which cannot be explained by the registration function  $f_{t,t+1}$ . In this study, a Gaussian process model is used to characterize the stationary component in the error term  $\varepsilon_{t+1}$ .

The rationale of the proposed formulation (Equation (1)) is illustrated in Figure 3. The image sequence model comes from the hypothesis that the thermal history of AM processes will be stable when the AM process is healthy. Furthermore, the melt pool images are also determined by the instantaneous printing direction. Therefore, the paper proposes to characterize the relationship between the two consecutive melt pool images using an image registration function to characterize the translational and rotational relationship between the two consecutive images. The best fitted rotational operation between the two images will be

compared with the instantaneous printing directional changes. Furthermore, any difference that cannot be explained in the image registration function will be included in the error term.

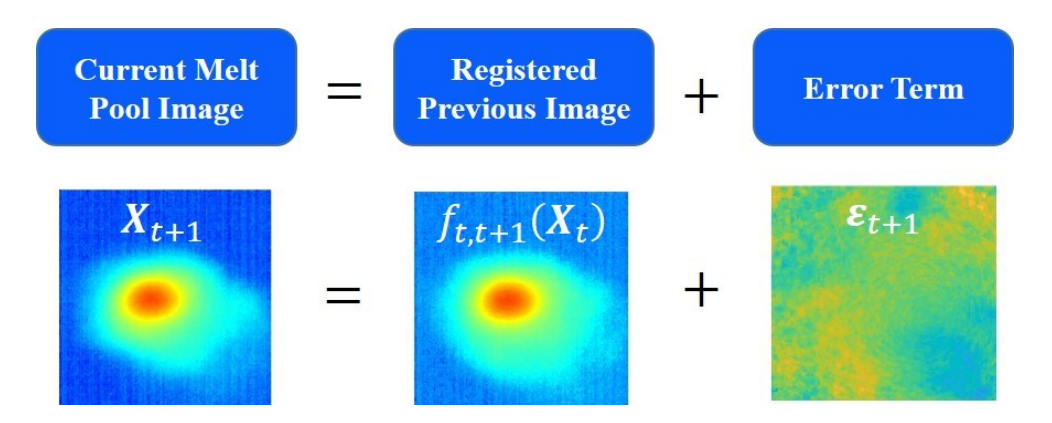


Figure 3: Melt pool image series formulation

### 3.2 Image Registration between Consecutive Images

In this paper, image registration is used to project  $X_t$  to  $X_{t+1}$  ( $t \in \mathcal{T}_l$ ) for the best alignment, which is characterized as the minimal mean squared error between the two images after registration. The registration function  $f_{t,t+1}$  can involve both translation and rotation operations of  $X_t$  to optimally fit  $X_{t+1}$ . Specifically, the translation operation signifies the magnitude of shift in a 2D coordinate system between  $X_t$  and  $X_{t+1}$ , whereas the rotation describes the orientation difference between  $X_t$  and  $X_{t+1}$ . The output of the image registration technique is defined as a 3×3 transformation matrix of  $\Omega_{t,t+1}$  in Equation (2),

$$\mathbf{\Omega}_{t,t+1} = \begin{bmatrix} a^{t,t+1} & b^{t,t+1} & 0\\ -b^{t,t+1} & a^{t,t+1} & 0\\ t_x^{t,t+1} & t_y^{t,t+1} & 1 \end{bmatrix}$$
(2)

where,  $t_x^{t,t+1}$  and  $t_y^{t,t+1}$  denote the number of pixels to shift  $X_t$  in the horizontal and vertical directions, respectively. In addition,  $a^{t,t+1}$  and  $b^{t,t+1}$  jointly specify the rotation operation, such that  $a^{t,t+1} = \cos q^{t,t+1}$  and  $b^{t,t+1} = \sin q^{t,t+1}$ , where  $q^{t,t+1}$  denotes the rotation angle of  $X_t$  about the origin of the image to best fit  $X_{t+1}$ . In an iterative procedure, the image registration algorithm is performed to minimize a pre-defined similarity metric (such as mean square error (MSE) of the images after registration). The image registration operations iteratively modify the operations to  $X_t$  to obtain a minimal MSE [32].

#### 3.3 Error Modeling based on Gaussian Process Models

The Gaussian Process (GP) model enables to characterize highly nonlinear covariance structure [33], [34] in the error term  $\varepsilon_{t+1}$  in Equation (1), as illustrated in Equation (3),

$$\varepsilon_{t+1} \sim GP(\beta_{t+1}, K((i,j), (i',j')) + \sigma_{t+1}^2 I_n)$$
(3)

Here, in the error term matrix  $\varepsilon_{t+1}$ , the row and column indices of the pixel are denoted as i and j, where i=1,2,3,...,I, and j=1,2,3,...,J.  $\beta_{t+1}$  denotes the intercept of the GP model.  $\sigma_{t+1}^2$  denotes the variation of the modeling error of  $\varepsilon_{t+1}$  and  $I_n$  is an identity matrix, which collectively identify the white noise error. The kernel function is represented by  $K(\cdot,\cdot)$ , which is used to characterize the covariance between the different locations in  $\varepsilon_{t+1}$ , such as (i,j) and (i',j'). Specifically, it determines how the response at each pixel is correlated with the responses at its neighboring pixels. The covariance function  $K(\cdot,\cdot)$  can be parameterized by various kernel functions. In this study, to characterize the spatial correlation in  $\varepsilon_{t+1}$ 's, the squared exponential kernel function is used as follows,

$$K((i,j),(i',j')|\sigma_L^{t,t+1},\sigma_F^{t,t+1}) = (\sigma_F^{t,t+1})^2 \exp\left(-\frac{1}{2}\frac{r^2}{(\sigma_L^{t,t+1})^2}\right)$$
(4)

where, r represents the Euclidean distance between the two pixels (i,j) and (i',j'), i.e.,  $r = \sqrt{(i-i')^2 + (j-j')^2}$ , as shown in Figure 4;  $\sigma_L^{t,t+1}$  denotes the characteristic length scale, and  $\sigma_F^{t,t+1}$  denotes the signal standard deviation [35].

The Quasi-Newton optimizer can be used for parameter estimation of the GP models. To accelerate the parameter estimation in the GP modeling for  $\varepsilon_{t+1}$ , the data sampling technique is adopted to the  $I \times J$  error matrix. This will serve to reduce the computational cost of GP models when the dimensionality of  $\varepsilon_{t+1}$  is high. Specifically, a pre-defined number s of pixels are randomly sampled from the error matrix  $\varepsilon_{t+1}$ , which are used as the response data in the GP model. The effect of the sample size s on the final anomaly detection performance and computational time is investigated in the case studies in section 4.

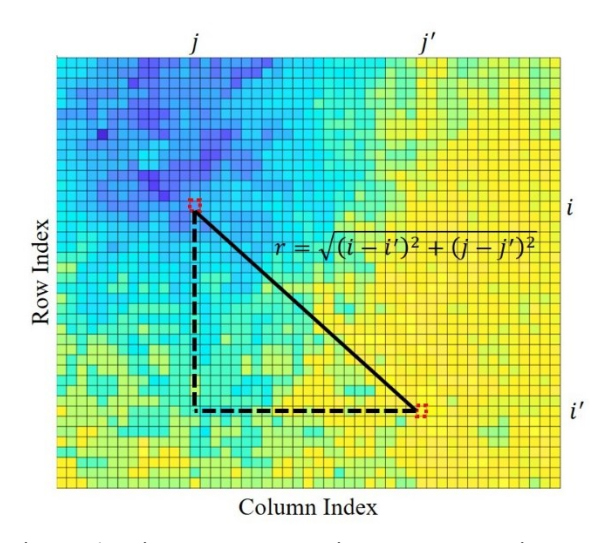


Figure 4: Distance measure in an error matrix  $\varepsilon_{t+1}$ 

### 3.4 Layer-wise Feature Extraction

The layer-wise thermal image series are characterized by extracting two groups of features. One group of features are extracted from the transformation matrix  $\Omega_{t,t+1}$  of image registration function, and another group is extracted from the estimated parameters from the GP models to characterize the error matrix  $\varepsilon_{t+1}$ .

### 3.4.1 Registration related Features

The image registration related features are extracted from the transformation matrix  $\Omega_{t,t+1}$  as presented in Equation (2), where the rotation and translation parameters can be determined as i) the angle of rotation

$$q^{t,t+1} = \tan^{-1} \left( \frac{b^{t,t+1}}{a^{t,t+1}} \right)$$
 (5)

and ii) Euclidian distance shifted from  $X_t$  to the registered image

$$ED^{t,t+1} = \sqrt{(t_x^{t,t+1})^2 + (t_y^{t,t+1})^2}$$
 (6)

The parameters of  $q^{t,t+1}$ , and  $ED^{t,t+1}$  are the two fitted features of image rotation and translation between image  $X_t$  and  $X_{t+1}$ , respectively.

The feature used to characterize the rotation operation, denoted as  $RO^{t+1}$ , can be determined by calculating the absolute difference between the theoretical and fitted angular changes between the consecutive melt pool images. The theoretical angular change  $\Delta\theta^{t,t+1}$  can be calculated from the printing

path by linear or circular interpolation using the coordinates in the g-code; and the rotation operation related feature can be calculated as the absolute difference between the theoretical and fitted angular changes, i.e.,

$$RO^{t+1} = |q^{t,t+1} - \Delta\theta^{t,t+1}| \tag{8}$$

Both features characterize the dynamic change in the melt pool image series, and their values should be very small when the AM process is stable. Therefore, the maximum values of both features are calculated to quantify the most extreme changes in the melt pool image series. Both registration related layer-wise features for anomaly detection can be calculated based on Equation (9) and (10),

$$F_l^1 = \max_{t \in T_l} \{ ED^{t,t+1} \} \tag{9}$$

$$F_l^2 = \max_{t \in \mathcal{T}_l} \{RO^{t+1}\} \tag{10}$$

where the layer-wise features of the l-th layer are denoted as  $F_l^1$  and  $F_l^2$ , which can be calculated by taking the maximum of the local registration related features in the fabrication of the l-th layer.

### 3.4.2 Error Modeling based Features

Using the estimated parameters of the GP models, the error modeling based features are extracted, including the absolute value of the intercept  $F_{l,t+1}^3 = |\beta_{t+1}|$ , and the variation and covariance related features, i.e.,  $F_{l,t+1}^4 = \sigma_{t+1}$ ,  $F_{l,t+1}^5 = \sigma_{t}^{t,t+1}$ , and  $F_{l,t+1}^6 = \sigma_{t}^{t,t+1}$ . Similar to the calculation of  $F_l^1$  and  $F_l^2$ , each GP model related feature quantifies the dynamics in the thermal history, where the larger the features are, the more unstable the melt pool image series will be. Therefore, to obtain the layer-wise features, the maximum value of each feature for the l-th layer is calculated as  $F_l^1 = \max_{t \in \mathcal{T}_l} \{F_{l,t}^i\}$ , where i = 3, 4, 5, 6 and  $\mathcal{T}_l$  represents the set of timestamps which are included in the fabrication of the l-th layer.

# 3.5 Anomaly Detection based on Layer-wise Features

Supervised learning methods can be used for layer-wise anomaly detection via training a classification model based on labeled historical data. The layer-wise labeling information can be obtained using post-process quality evaluation such as X-ray CT scanning. Specifically, a layer is labeled as healthy if it does not include a porosity, and one is labeled as unhealthy if it contains at least one porosity. It should be noted

that various machine learning algorithms can be applied for layer-wise anomaly detection in real time. In this study, the support vector machine (SVM) method is used due to its flexibility in learning the boundary by incorporating diversified kernel functions. By leveraging a historical data set with labeling information, an SVM classifier can be trained by finding the hyperplane that best separates all data points of different classes, and the complexity of the hyperplane can be determined by cross validation [36].

# 4. Case Study

### 4.1 Experimental setup

The Laser Engineered Net Shaping (LENS) process is one of the most widely used DLD processes and is thus used to validate the effectiveness of the proposed methodology. The LENS 750 machine used in the case study is equipped with a co-axial pyrometer camera (Stratonics, Inc.) to capture the melt pool image series. More information about the experimental setup can be found in [10], [37]. The feedstock material used was Ti-6AL-4V powder. To examine the robustness of the proposed method to different printing trajectories, two parts with different geometries (i.e., one thin wall and one cylindrical shaped part) were fabricated (as illustrated in Figure 5). The key process parameters of the two specimens are summarized in Table 1.



Figure 5: Additively fabricated parts: a) thin wall, and b) cylinder part.

During the specimen fabrication, the melt pool images were captured using the co-axial pyrometer camera, producing melt pool images in the matrix form of 480×752, with each pixel value represents the temperature measurement at that location. Some melt pool image examples from one layer of both two parts are illustrated in Figure 2. It can be observed that for the thin wall specimen, all the melt pools within one layer have the identical orientation due to its unidirectional printing path. In addition, the cylindrical

specimen demonstrates diversified orientation in the melt pool images collected from the layer-wise fabrication. For example, during the printing of the perimeter of the cylinder, the melt pool orientation is varying continuously over time, and thus needs to be taken into account in the melt pool image series modeling for anomaly detection. After the build of the parts, the porosity inside the structure was evaluated using the X-ray CT scanning procedure (Skyscan 1172), and the minimum size of a detectable pore was set to  $0.05\mu m$ .

Table 1: Process parameters for fabricating the two specimens.

Parameters	Thin wall	Cylinder		
Scan speed	30 inch/min	40 inch/min		
Powder feed rate	4 rpm	3 rpm		
Hatch spacing	0.02 inch	0.02 inch		
Power	300 W	300 W		
Layer thickness	0.02 inch	0.015 inch		
Nozzle diameter	0.035 inch	0.035 inch		
Infill pattern	-	Unidirectional (180° rotation between layers)		
Total number of layers in the build	60	69		
Number of abnormal layers in the build	26	58		
Number of thermal images collected	1557	2827		

### 4.2 Benchmark method selection

One group of potential methods for benchmark analysis is time series models (such as autoregressive modeling [38]). The stochastic nature of the temporal sequenced data can be characterized and the one-step ahead prediction error can be used for process monitoring [39], [40]. However, one most important assumption of most time series analysis methods is stationarity, where the mean, variance, and autocorrelation structure do not change over time [41]. Unfortunately, this assumption does not hold in the layer-wise melt pool image series since the relationship between consecutive images are essentially dynamic and cannot be properly characterized using a time series model.

The layer-wise anomaly detection method proposed by Seifi et al. [10] was used as the benchmark method, which is the most recently published layer-wise anomaly detection methodology for DLD processes. In the benchmark method, multi-linear principal component analysis (MPCA) was leveraged to reduce the dimension of the thermal images. Subsequently, the volume of the convex hull formed by the extracted MPCs extracted from each layer is used as one layer-wise feature to quantify the stability of the thermal history within one layer. On the other hand, the maximum value of the residual norm of the MPCA modeling within a layer is used any the second feature for layer-wise anomaly detection. The method demonstrates superior layer-wise anomaly detection performance when compared with its benchmark methods for the thin wall specimen fabrication.

#### 4.3 Evaluation procedure

To compare the performance of the proposed and benchmark method, the thermal history of two DLD fabrication have been used, i.e., one is a thin wall and the other is a cylindrical specimen, leading to two separate datasets. The two datasets were trained and evaluated separately based on the following procedure. First, each data set was randomly split into the training set (80%) and testing set (20%), and both the proposed method and the benchmark method were implemented separately for model training and performance evaluation.

For the proposed feature extraction, only the translational operator (i.e.,  $ED^{t,t+1}$ ) was extracted as the registration related feature from the thin wall dataset due to the unidirectional printing path used. On the other hand, for the cylindrical part dataset, both translational (i.e.,  $ED^{t,t+1}$ ) and rotational operators (i.e.,  $RO^{t+1}$ ) were extracted as the registration related features. The error modeling related features extracted are the same for both datasets. Subsequently, their corresponding layer-wise features were calculated and the SVM classifiers were trained based on the layer-wise labels.

200 replications of the performance evaluation were conducted by performing the random data split 200 times and evaluating the average performance. The recall, precision, Fscore, and overall accuracy are reported as the performance metrics of the two methods, which can be calculated as follows:

$$Recall = \frac{TP}{TP + FN} \tag{11}$$

$$Precision = \frac{TP}{TP + FP}$$
 (12)

$$Fscore = 2 \times \frac{Precision \times Recall}{Precision + Recall}$$
 (13)

$$Accuracy = \frac{TP + TN}{TP + TN + FP + FN}$$
 (14)

where True-Positive (TP) denotes the unhealthy layers which are predicted accurately as unhealthy, whereas True-Negative (TN) represents the healthy layers which are accurately predicted as healthy. On the other hand, False-Negative (FN) denotes inaccurate prediction of unhealthy layers as healthy, while False-Positive (FP) represents inaccurate prediction of the layers which are healthy but predicted as unhealthy. In each iteration, the TP, TN, FN, and FP values were obtained by comparing the predicted labels and the ground truth labels from the X-ray CT inspection based on the testing data set. The Fscore is the harmonic mean of precision and recall, and the overall accuracy is calculated by dividing the total correct classifications by the total number of layers evaluated. In this paper, similar to [10], the Fscore value is used as the major metric for performance comparison.

#### 4.4 Results and discussion

The mean of the performance metrics of both the proposed and benchmark methods are summarized in Table 2. To test the effects of the sample size *s* used in fitting the GP model for the error matrix, a variety of different sample size values were evaluated. It can be observed that the proposed method and the benchmark method demonstrate comparable average Fscore performance in the layer-wise anomaly detection for the thin wall specimen. However, the proposed method significantly outperforms the benchmark method for the cylindrical shaped part. It can be observed that the Fscore values of the proposed method using different *s* values are universally higher (approximately 6% higher) than the benchmark method, and the overall accuracy of the proposed method is approximately 10% higher than the benchmark method. This significant improvement is mainly because the proposed method takes the printing trajectory

information into account in the melt pool image series modeling. Therefore, the proposed method is capable of layer-wise anomaly detection for complex geometry/printing paths.

Table 2: Result summary for performance comparison

Proposed method							Benchmark	
		s = 50	s=100	s = 150	s=200	s=300	s = 400	method
Thin wall	Accuracy	93.54%	93.17%	93.00%	93.92%	93.12%	93.25%	94.67%
	Precision	94.75%	91.88%	91.63%	93.64%	91.85%	92.50%	95.91%
	Recall	91.20%	93.58%	93.58%	93.68%	93.68%	93.58%	90.98%
	Fscore	92.36%	92.10%	91.97%	93.06%	92.10%	92.38%	93.24%
Cylinder	Accuracy	84.29%	84.21%	83.96%	83.93%	83.11%	83.21%	73.60%
	Precision	84.97%	84.96%	84.86%	84.85%	84.76%	84.78%	81.46%
	Recall	99.18%	98.94%	98.72%	98.68%	97.76%	97.89%	88.05%
	Fscore	91.26%	91.18%	91.02%	91.00%	90.52%	90.59%	84.12%

There are three possible reasons for observed misclassification of both the proposed and the benchmark methods. First, the discrete data sampling limits the data acquisition of the thermal history, which may lead to missed thermal images when the actual anomaly occurs. Second, the X-ray CT scanning characterization may be subject to noise and error. Third, the proposed anomaly detection method does not consider effects of re-melting, which can potentially remove some of the porosities generated in the previous layer during the deposition of the consecutive layers.

The computational time of the proposed method with different sample size values *s* in the GP modeling phase is demonstrated in Figure 6, where the average layer-wise computation time and the layer-wise build time is visualized. The processor used to evaluate the computation efficiency was Intel® Core<sup>TM</sup> Processor i7-7700 CPU @ 3.60GHz. It can be observed that the computation time for the cylinder specimen is significantly longer than the thin wall specimen due to the additional operation in the registration phase (i.e., rotation operation) to accommodate complex printing trajectory. In addition, it can be observed that reducing the sample size used in the GP modeling phase can significantly reduce the computation time, while not significantly affecting the anomaly detection results (as illustrated in Table 2). It is also worth noting that in all the tested scenarios the computation for layer-wise anomaly detection takes significantly shorter than its corresponding layer-wise fabrication for both specimens. Therefore, the proposed method

is computationally efficient and thus can facilitate *in-situ* layer-wise anomaly detection and potential process control.

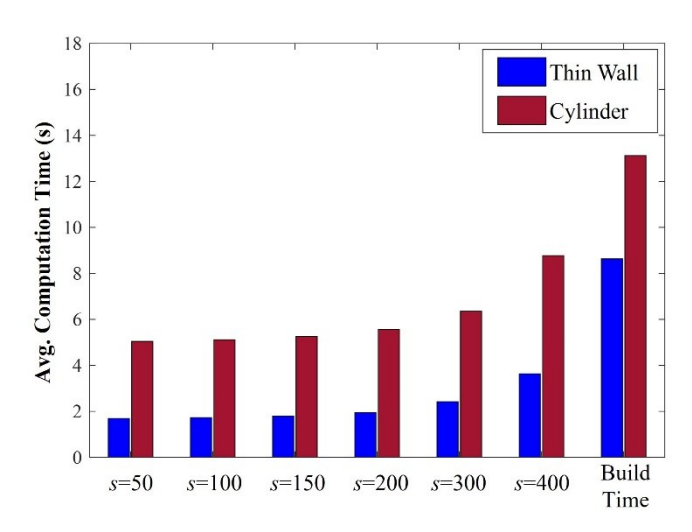


Figure 6: Average layer-wise computation time given different sample size s used in the GP model.

#### 5. Conclusion

Direct laser deposition (DLD) is a widely used metal-based additive manufacturing technology in fabricating functional components for mission critical applications. However, the lack of repeatability in the additively fabricated parts is one of the major challenges that hinders broader industrial applications of DLD processes. Possible quality issues, such as internal porosity, deformation, and cracking, can lead to significantly compromised mechanical properties. Comprehensive studies including data-driven methods have been focused on local characterization for anomaly detection based on individual thermal images. A layer-wise thermal image modeling framework can take into account the printing trajectory information to characterize the complex spatio-temporal relationship within the image series, which can achieve improved anomaly detection results. In this paper, the layer-wise thermal images are formulated as an image series, and the image registration method is used to quantify the dynamic relationship between consecutively observed thermal images. In addition, Gaussian process (GP) models are used to characterize the error term which is left unexplained by the registration operation. Multiple layer-wise features are extracted from the registration operation and GP model-based error modeling, respectively. The support vector machine

classifier is trained based on historical data and used for *in-situ* layer-wise anomaly detection based on the extracted layer-wise features. Case studies based on a thin wall and a cylindrical shaped specimen fabrication using a DLD process are used to validate the proposed methodology. The proposed method also demonstrates competitive performance when comparing with the benchmark methods for layer-wise anomaly detection.

A couple of research topics remain open for future work. First, more sophisticated geometric parts, such as freeform parts, will be used to test the performance of the proposed. Second, the proposed methodology is limited to training one model for one identical set of AM process parameters, making the proposed method quite expensive for data collection. Therefore, transfer learning algorithm and domain adaptation methods can be adopted to combine the process data collected using different process parameters or even different AM machines for part certification and anomaly detection. Last but not the least, the prediction of mechanical behavior of the AM parts is critical to AM users. Therefore, it is necessary to link the detected anomaly characteristics with the durability and the performance of the fabricated AM parts.

#### **Acknowledgments**

Research was partially sponsored by the Army Research Laboratory and was accomplished under Cooperative Agreement Number W911NF-15-2-0025. The views and conclusions contained in this document is those of the authors and should not be interpreted as representing the official policies, either expressed or implied, of the Army Research Laboratory or the U.S. Government. The U.S. Government is authorized to reproduce and distribute reprints for Government purposes notwithstanding any copyright notation herein. In addition, this work was partially sponsored by the National Science Foundation (No. CMMI-2046515).

#### References

[1] S. M. Thompson, L. Bian, N. Shamsaei, and A. Yadollahi, "An overview of Direct Laser

Deposition for additive manufacturing; Part I: Transport phenomena, modeling and diagnostics,"

- Addit. Manuf., vol. 8, pp. 36–62, 2015, doi: 10.1016/j.addma.2015.07.001.
- [2] L. Scime, D. Siddel, S. Baird, and V. Paquit, "Layer-wise anomaly detection and classification for powder bed additive manufacturing processes: A machine-agnostic algorithm for real-time pixelwise semantic segmentation," *Addit. Manuf.*, vol. 36, no. March, p. 101453, 2020, doi: 10.1016/j.addma.2020.101453.
- [3] H. Kim, Y. Lin, and T. L. B. Tseng, "A review on quality control in additive manufacturing," *Rapid Prototyp. J.*, vol. 24, no. 3, pp. 645–669, 2018, doi: 10.1108/RPJ-03-2017-0048.
- [4] N. Shamsaei, A. Yadollahi, L. Bian, and S. M. Thompson, "An overview of Direct Laser Deposition for additive manufacturing; Part II: Mechanical behavior, process parameter optimization and control," *Addit. Manuf.*, vol. 8, pp. 12–35, 2015, doi: 10.1016/j.addma.2015.07.002.
- [5] C. Wang, X. P. Tan, S. B. Tor, and C. S. Lim, "Machine learning in additive manufacturing: State-of-the-art and perspectives," *Addit. Manuf.*, vol. 36, no. January, p. 101538, 2020, doi: 10.1016/j.addma.2020.101538.
- [6] M. Khanzadeh, S. Chowdhury, M. Marufuzzaman, M. A. Tschopp, and L. Bian, "Porosity prediction: Supervised-learning of thermal history for direct laser deposition," *J. Manuf. Syst.*, vol. 47, no. April, pp. 69–82, 2018, doi: 10.1016/j.jmsy.2018.04.001.
- [7] M. Khanzadeh, W. Tian, A. Yadollahi, H. R. Doude, M. A. Tschopp, and L. Bian, "Dual process monitoring of metal-based additive manufacturing using tensor decomposition of thermal image streams," *Addit. Manuf.*, vol. 23, no. July, pp. 443–456, 2018, doi: 10.1016/j.addma.2018.08.014.
- [8] Q. Tian, S. Guo, E. Melder, L. Bian, and W. Guo, "Deep Learning-based Data Fusion Method for In-Situ Porosity Detection in Laser-based Additive Manufacturing," *J. Manuf. Sci. Eng.*, vol. 143, no. April, pp. 1–38, 2020, doi: 10.1115/1.4048957.
- [9] H. Yan, M. Grasso, K. Paynabar, and B. M. Colosimo, "Real-time Detection of Clustered Events in Video-imaging data with Applications to Additive Manufacturing," pp. 1–40, 2020.
- [10] S. H. Seifi, W. Tian, H. Doude, M. A. Tschopp, and L. Bian, "Layer-Wise Modeling and Anomaly

- Detection for Laser-Based Additive Manufacturing," *J. Manuf. Sci. Eng. Trans. ASME*, vol. 141, no. 8, pp. 1–12, 2019, doi: 10.1115/1.4043898.
- [11] G. Chen *et al.*, "A pore morphological study of gas-atomized Ti-6Al-4V powders by scanning electron microscopy and synchrotron X-ray computed tomography," *Powder Technol.*, vol. 330, pp. 425–430, 2018, doi: 10.1016/j.powtec.2018.02.053.
- [12] M. Seifi *et al.*, "Progress Towards Metal Additive Manufacturing Standardization to Support Qualification and Certification," *JOM*, vol. 69, no. 3, 2017, doi: 10.1007/s11837-017-2265-2.
- [13] K. Jurrens and Energetics Incorporated, "Measurement Science Roadmap for Metal-Based Additive Manufacturing," *Addit. Manuf.*, p. 86, 2013.
- [14] C.-J. Bae, A. B. Diggs, and A. Ramachandran, "Quantification and certification of additive manufacturing materials and processes," in *Additive Manufacturing*, Elsevier, 2018, pp. 181–213.
- [15] A. Du Plessis, S. G. Le Roux, G. Booysen, and J. Els, "Quality Control of a Laser Additive Manufactured Medical Implant by X-Ray Tomography," *3D Print. Addit. Manuf.*, vol. 3, no. 3, pp. 175–182, 2016, doi: 10.1089/3dp.2016.0012.
- [16] F. Bernier, R. Tahara, and M. Gendron, "Additive manufacturing powder feedstock characterization using X-ray tomography," *Met. Powder Rep.*, vol. 73, no. 3, pp. 158–162, 2018, doi: 10.1016/j.mprp.2018.01.002.
- [17] C. Gobert, A. Kudzal, J. Sietins, C. Mock, J. Sun, and B. McWilliams, "Porosity segmentation in X-ray computed tomography scans of metal additively manufactured specimens with machine learning," *Addit. Manuf.*, vol. 36, no. August 2019, p. 101460, 2020, doi: 10.1016/j.addma.2020.101460.
- [18] V. Cnudde, A. Cwirzen, B. Masschaele, and P. J. S. Jacobs, "Porosity and microstructure characterization of building stones and concretes," *Eng. Geol.*, vol. 103, no. 3–4, pp. 76–83, 2009, doi: 10.1016/j.enggeo.2008.06.014.
- [19] G. F. Andriani and N. Walsh, "Fabric, porosity and water permeability of calcarenites from Apulia (SE Italy) used as building and ornamental stone," *Bull. Eng. Geol. Environ.*, vol. 62, no. 1, pp.

- 77–84, 2003, doi: 10.1007/s10064-002-0174-1.
- [20] B. M. Colosimo and M. Grasso, "Spatially weighted PCA for monitoring video image data with application to additive manufacturing," *J. Qual. Technol.*, vol. 50, no. 4, pp. 391–417, 2018, doi: 10.1080/00224065.2018.1507563.
- [21] L. Scime and J. Beuth, "Anomaly detection and classification in a laser powder bed additive manufacturing process using a trained computer vision algorithm," *Addit. Manuf.*, vol. 19, pp. 114–126, 2018, doi: 10.1016/j.addma.2017.11.009.
- [22] B. Lane *et al.*, "Transient Laser Energy Absorption, Co-axial Melt Pool Monitoring, and Relationship to Melt Pool Morphology," *Addit. Manuf.*, vol. 36, no. August, p. 101504, 2020, doi: 10.1016/j.addma.2020.101504.
- [23] J. A. Mitchell, T. A. Ivanoff, D. Dagel, J. D. Madison, and B. Jared, "Linking pyrometry to porosity in additively manufactured metals," *Addit. Manuf.*, vol. 31, no. July 2019, 2020, doi: 10.1016/j.addma.2019.100946.
- [24] D. Hu and R. Kovacevic, "Sensing, modeling and control for laser-based additive manufacturing," *Int. J. Mach. Tools Manuf.*, vol. 43, no. 1, pp. 51–60, 2003, doi: 10.1016/S0890-6955(02)00163-3.
- [25] S. Guo, W. "Grace" Guo, and L. Bain, "Hierarchical spatial-temporal modeling and monitoring of melt pool evolution in laser-based additive manufacturing," *IISE Trans.*, vol. 52, no. 9, pp. 977– 997, 2020, doi: 10.1080/24725854.2019.1704465.
- [26] W. "Grace" Guo, Q. Tian, S. Guo, and Y. Guo, "A physics-driven deep learning model for process-porosity causal relationship and porosity prediction with interpretability in laser metal deposition," *CIRP Ann.*, vol. 69, no. 1, pp. 205–208, 2020, doi: 10.1016/j.cirp.2020.04.049.
- [27] A. du Plessis *et al.*, "X-ray computed tomography inspection in metal additive manufacturing: the role of witness specimens," *Struct. Integr. Addit. Manuf. Mater. Parts*, 2020.
- [28] M. Mahmoudi, A. A. Ezzat, and A. Elwany, "Layerwise Anomaly Detection in Laser Powder-Bed Fusion Metal Additive Manufacturing," *J. Manuf. Sci. Eng. Trans. ASME*, vol. 141, no. 3, pp. 1–13, 2019, doi: 10.1115/1.4042108.

- [29] M. Mani, B. M. Lane, M. A. Donmez, S. C. Feng, and S. P. Moylan, "A review on measurement science needs for real-time control of additive manufacturing metal powder bed fusion processes," *Int. J. Prod. Res.*, vol. 55, no. 5, pp. 1400–1418, 2017.
- [30] J. M. Waller, B. H. Parker, K. L. Hodges, E. R. Burke, J. L. Walker, and E. R. Generazio, "Nondestructive evaluation of additive manufacturing," *Natl. Aeronaut. Sp. Adm.*, 2014.
- [31] S. H. Seifi, A. Yadollahi, W. Tian, H. Doude, V. H. Hammond, and L. Bian, "In Situ Nondestructive Fatigue-Life Prediction of Additive Manufactured Parts by Establishing a Process— Defect-Property Relationship," *Adv. Intell. Syst.*, p. 2000268, 2021.
- [32] L. G. Brown, "A survey of image registration techniques," *ACM Comput. Surv.*, vol. 24, no. 4, pp. 325–376, 1992.
- [33] C. E. Rasmussen, C. K. I. Williams, G. Processes, M. I. T. Press, and M. I. Jordan, *Gaussian Processes for Machine Learning*. 2006.
- [34] C. E. Rasmussen and H. Nickisch, "Gaussian processes for machine learning (GPML) toolbox," *J. Mach. Learn. Res.*, vol. 11, pp. 3011–3015, 2010.
- [35] M. Seeger, "Gaussian processes for machine learning.," *Int. J. Neural Syst.*, vol. 14, no. 2, pp. 69–106, 2004, doi: 10.1142/S0129065704001899.
- [36] J. Friedman, T. Hastie, and R. Tibshirani, *The elements of statistical learning*, vol. 1, no. 10. Springer series in statistics New York, 2001.
- [37] M. Khanzadeh, S. Chowdhury, M. A. Tschopp, H. R. Doude, M. Marufuzzaman, and L. Bian, "Insitu monitoring of melt pool images for porosity prediction in directed energy deposition processes," *IISE Trans.*, vol. 51, no. 5, pp. 437–455, 2019, doi: 10.1080/24725854.2017.1417656.
- [38] P. Kokoszka and M. Reimherr, "Determining the order of the functional autoregressive model," *J. Time Ser. Anal.*, vol. 34, no. 1, pp. 116–129, 2013.
- [39] L. Xiang and F. Tsung, "Statistical monitoring of multi-stage processes based on engineering models," *IIE Trans.*, vol. 40, no. 10, pp. 957–970, 2008.
- [40] W. Tian, R. Jin, T. Huang, and J. A. Camelio, "Statistical process control for multistage processes

with non-repeating cyclic profiles," IISE Trans., vol. 49, no. 3, pp. 320-331, 2017.

[41] W. W. S. Wei, "Time series analysis," in *The Oxford Handbook of Quantitative Methods in Psychology: Vol. 2*, 2006.